



Cite this: *Mater. Adv.*, 2023, 4, 2981

## Removal of methyl red from wastewater using a NiO@*Hyphaene thebaica* seed-derived porous carbon adsorbent: kinetics and isotherm studies†

Abdelaal S. A. Ahmed, \*<sup>a</sup> Moustafa M. S. Sanad, <sup>b</sup> Ahmed Kotb,<sup>a</sup> Ahmed N. R. M. Negm<sup>a</sup> and Mohamed H. Abdallah<sup>a</sup>

In this study, the adsorption of methyl red (MR) dye from wastewater on nickel oxide (NiO) doped in porous carbon derived from *Hyphaene thebaica* (HT) seeds (NiO@HT derived C) as an adsorbent material was investigated. The prepared NiO@HT derived C was characterised by Fourier transform infrared spectroscopy (FTIR), X-ray diffraction (XRD), field emission scanning electron microscopy (FESEM), and X-ray photoelectron spectroscopy (XPS). Moreover, the effects of solution pH, contact time, amount of the adsorbent, and the initial concentration of MR on the adsorption efficiency were consistently examined. The adsorption capacity of NiO@HT derived C at room temperature ( $25\text{ }^{\circ}\text{C} \pm 2$ ) could reach  $129.87\text{ mg g}^{-1}$  in an acidic medium after shaking for 60 min. Furthermore, the adsorption kinetics and isotherms of adsorption were investigated. The results indicated that the adsorption isotherm of reactive MR on the NiO@HT derived C surface follows the Langmuir isotherm model, which revealed that the adsorption of MR is a chemisorption process. On the other hand, the kinetic data fit well with the pseudo-second-order kinetic model, indicating that both NiO@HT derived C and MR influence the adsorption process.

Received 10th May 2023,  
Accepted 13th June 2023

DOI: 10.1039/d3ma00226h

rsc.li/materials-advances

## 1. Introduction

Dyes are chemical molecules that are unpleasant and hazardous to the environment.<sup>1</sup> Usually, dyes are extensively used in many industrial applications, such as cosmetics, plastics, paper, printing, pharmaceuticals, and textiles.<sup>2</sup> Textile industries are the greatest generators of dye wastewater that is discharged into the environment.<sup>3,4</sup> Removing or minimizing dyes from wastewater has attracted attention worldwide due to the emission hazards, which are harmful to humans and the aquatic environment.<sup>2,5,6</sup> Even if a small amount of coloured dye is discharged into the water, it is visually unappealing.<sup>7</sup> The dyes used in industries are generally classified as cationic, anionic, or natural dyes.<sup>8</sup> MR is an anionic azo dye that is important for various industrial and laboratory purposes; however, the presence of MR in water can cause health issues related to stomach, eye and skin irritation.<sup>9,10</sup> Furthermore, the presence of benzene rings renders MR mutagenic under aerobic conditions and results in low biodegradability.<sup>11</sup> Moreover, the presence of MR in water may cause digestive tract,

eye and skin discomfort.<sup>12</sup> Thus, there is an urgent need to remove MR from the polluted water before it is discharged into the environment. It is possible to remove colours from effluents using chemical, physical, or biological methods.<sup>13–15</sup> Various techniques such as coagulation,<sup>16</sup> photocatalytic oxidation,<sup>17</sup> adsorption,<sup>12</sup> ozone treatment, and others have been employed for recovering dyes from wastewater. Among all, the adsorption process is currently considered the most utilized process for the efficient removal of dyes from wastewater due to its various advantages such as ease of use, low cost, and relatively high efficiency.<sup>2</sup> Choosing an appropriate adsorbent plays a key role in determining the total performance of the adsorption process. To date, various adsorbent materials, such as waste biomass<sup>9,18–20</sup> and activated carbon,<sup>18</sup> have been used for MR adsorption. Due to their large surface area and potent physical and chemical influences on the adsorption of dye effluents, metal oxide nanoparticles have been widely exploited as adsorbents toward synthetic dyes from wastewater in the last few decades.<sup>21,22</sup> Nickel oxide (NiO) is an important transition-metal oxide widely used in various applications such as solar cells,<sup>23</sup> energy storage systems,<sup>24</sup> and catalysis<sup>25</sup> due to its high chemical and thermal stability, and eco-friendly nature. For wastewater treatment, NiO is also widely used as an adsorbent for synthetic dyes.<sup>26</sup> For example, Riaz *et al.*<sup>26</sup> reported that NiO nanoparticles prepared by a green hydrothermal method showed an effective adsorption toward methyl orange (MO) with a maximum adsorption capacity

<sup>a</sup> Chemistry Department, Faculty of Science, Al-Azhar University, Assiut 71524, Egypt. E-mail: abdelaalsaiyd@gmail.com, abdelaalsaiyd@azhar.edu.eg

<sup>b</sup> Central Metallurgical Research and Development Institute, P.O. Box 87 Helwan, 11421, Cairo, Egypt

† Electronic supplementary information (ESI) available. See DOI: <https://doi.org/10.1039/d3ma00226h>



of  $97.56 \text{ mg g}^{-1}$  at pH 4. Furthermore, Song *et al.*<sup>27</sup> revealed that NiO nanosheets have high adsorptive affinity toward brilliant red X-3B, Congo red and fuchsine acid with maximum adsorption capabilities of  $30.4 \text{ mg g}^{-1}$ ,  $35.15 \text{ mg g}^{-1}$  and  $22 \text{ mg g}^{-1}$ , respectively. However, their overall adsorption efficiency still needs to be enhanced.<sup>28</sup> Integrating NiO nanoparticles with porous carbon materials is an effective strategy due to the synergistic effect.<sup>29</sup> Due to their abundant availability with almost zero cost, agricultural wastes have received intensive attention as precursors for the preparation of porous carbon for various environmental applications including wastewater treatment.<sup>30</sup> From the standpoint of waste management, converting bio-waste materials into porous carbon is a promising strategy for wastewater treatment.<sup>31,32</sup> In Egypt, there are numerous agricultural bio-waste items that are typically burned or dumped into the environment, which causes environmental contamination and subsequent health risks. These agricultural wastes could be a resource for the synthesis of porous carbon because they come from hardwood species with lignocellulosic character. Utilizing agricultural waste for the preparation of porous carbon is a promising way to produce cheap and efficient adsorbents and a potential alternative for solving the environmental problems of Egypt. In the Nile Valley governorate of Egypt and Sub-Saharan Africa, *Hyphaene thebaica* (HT) is a famous fruit that belongs to the Arecaceae family. The *Hyphaene thebaica* fruit is a solid fruit with a solid core, and the outside layer is edible. Due to the high percentage of waste produced from this fruit (>80% of the fruit's weight), it is highly recommended to find a way to make use of such waste materials, which will be important in economic and environmental aspects.<sup>33</sup> Herein, we used HT seeds as a source of porous carbon to prepare a NiO@HT-derived C composite to be utilized as an adsorbent for MR removal from aqueous solutions. The various parameters that affect the adsorption efficiency, such as pH, contact time, and dye concentration, were investigated. Moreover, the adsorption kinetics and isotherms were also investigated. The estimated data revealed high adsorption affinity of the NiO@HT-derived C composite toward MR, with an adsorption capacity of  $129.87 \text{ mg g}^{-1}$  at room temperature, which is

much better than that previously reported in the literature. According to our knowledge, this is the first time that this composite is prepared and utilized for wastewater treatment.

## 2. Experimental section

### 2.1. Preparation of adsorbents

*Hyphaene thebaica* fruits were obtained from the local market in New Valley Governorate, Egypt. The nickel oxide dispersed into HT-derived C (NiO@HT-derived C) was prepared as described in the scheme shown in Fig. 1. The whole process involves three steps: (i) a pre-treatment step, where the HT species was initially washed repeatedly with distilled water to remove soluble compounds and dust. After that, HT species was dried in an oven at  $100 \text{ }^\circ\text{C}$  for 8 h, followed by grinding with an electric grinder and screening through a 50 mesh screen. Then, the HT powder was bathed in boiling water for 8 h to remove the soluble impurities and finally dried at  $100 \text{ }^\circ\text{C}$  overnight. (ii) Adsorption of  $\text{Ni}^{2+}$  ions on the HT powder: 1.0 g of the dried HT powder was immersed in 100 mL of an aqueous solution of 0.1 M  $\text{Ni}(\text{NO}_3)_2$  under a magnetic stirrer for 3 h. Subsequently, 50 mL of a 2 M  $\text{NH}_4\text{OH}$  solution was stepwise dropped into the mixture and kept under a magnetic stirrer for 3 h at  $80 \text{ }^\circ\text{C}$ . The suspension was thoroughly washed with DI water and ethanol to obtain the  $\text{Ni(OH)}_2/\text{HT}$  composite; and (iii) the obtained composite ( $\text{Ni(OH)}_2/\text{HT}$ ) was subjected to carbonization at  $500 \text{ }^\circ\text{C}$  for 2 h at a heating rate of  $5 \text{ }^\circ\text{C min}^{-1}$ . The prepared NiO@HT-derived C was thoroughly washed with dilute HCl and distilled water until the pH reached 7, followed by drying at  $80 \text{ }^\circ\text{C}$  overnight to be ready for adsorption studies. The HT-derived C material was prepared using the same steps used for the NiO@HT-derived C composite except immersing in  $\text{Ni}^{2+}$  solution. The dried prepared materials were subjected to physicochemical characterization and adsorption studies.

### 2.2. Batch adsorption experiments

Batch adsorption of MR dye was performed in a 50 mL dark bottle with a magnetic stirrer. For all tests, 0.03 g of adsorbent

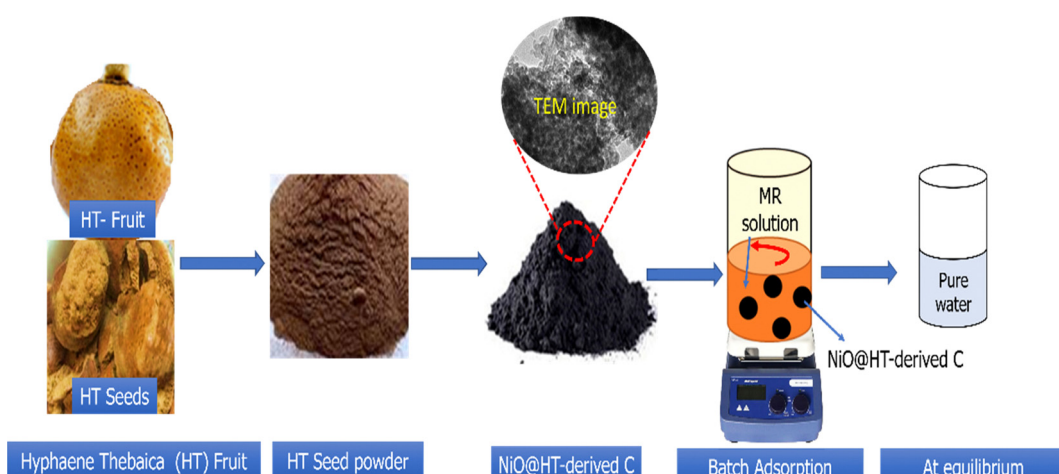


Fig. 1 Scheme for the preparation of the NiO@HT-derived C composite.



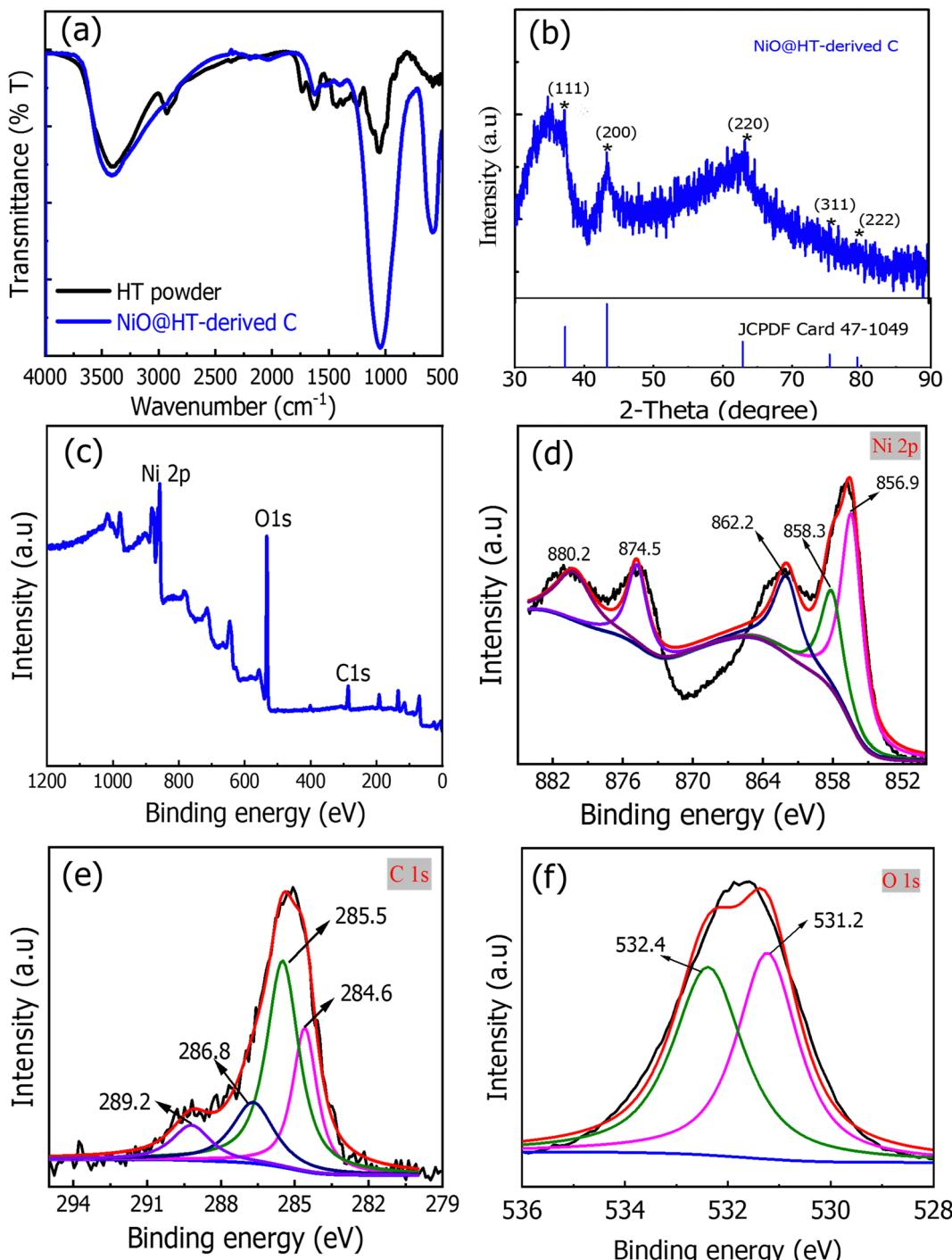


Fig. 2 (a) XRD pattern and (b) FT-IR spectra of the NiO@HT-derived C composite. (c–f) XPS spectra of the NiO@HT-derived C composite [(c) survey scan, (d) Ni2p, (e) C1s, and (f) O1s].

material was mixed with 25 mL of MR dye solution at an initial concentration of  $50 \text{ mg L}^{-1}$ . The solution pH was adjusted by hydrochloric acid (HCl) and sodium hydroxide (NaOH) solutions with concentrations of 0.1 M. The influence of pH, adsorbent dose, contact time, and the initial dye concentration on MR dye removal was examined. The remaining concentration of the MR dye was measured using a UV-visible spectrophotometer at a wavelength of 520 nm. Each adsorption

experiment was carried out in triplicate, and the average values with the related standard deviations (SD) were plotted. The percent removal ( $R\%$ ) of the MR dye was determined using eqn (1).

$$R(\%) = \frac{C_0 - C_e}{C_0} \times 100 \quad (1)$$

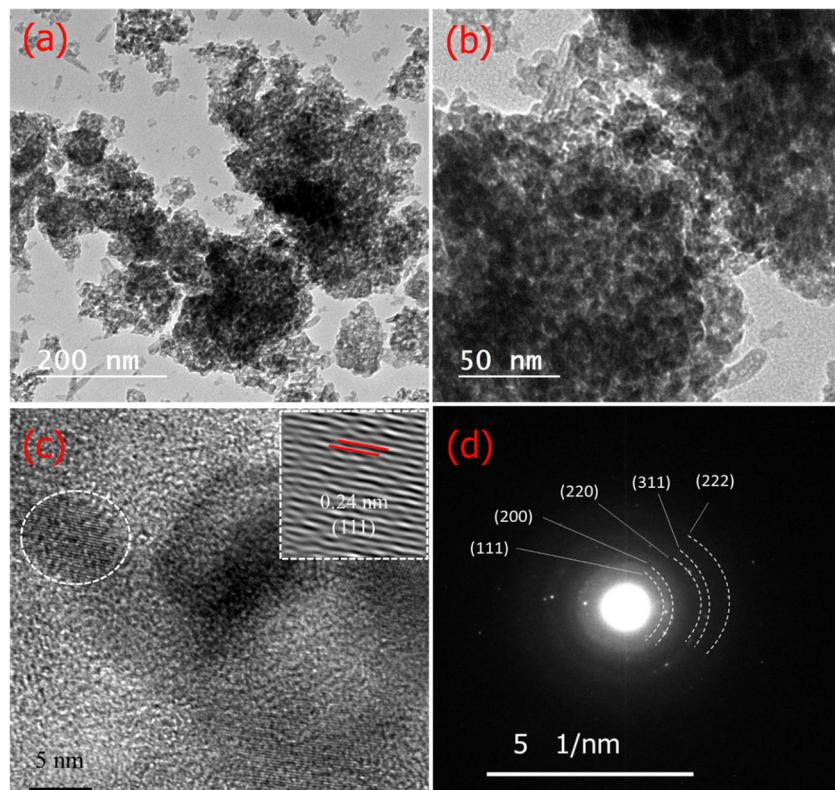


Fig. 3 (a and b) TEM, (c) HRTEM images, and (d) SAED pattern of the NiO@HT-derived C composite.

where  $C_0$  and  $C_e$  are the initial and final concentrations of the MR dye ( $\text{mg L}^{-1}$ ), respectively.

The adsorption capacity ( $q_e$ ) was measured using eqn (2).

$$q_e = \frac{(C_0 - C_e)}{M} V \quad (2)$$

where  $V$  is the volume of dye solution (L) and  $M$  is the weight of the adsorbent (g).

### 2.3. Adsorption kinetics and isotherms

The adsorption kinetics of the MR dye were performed by mixing 0.03 g of NiO@HT-derived C composite with 25 mL of dye solution ( $50 \text{ mg L}^{-1}$ , pH = 2.5, room temperature); the mixtures were kept under a magnetic stirrer for various contact times (5–120 min). The adsorption isotherms were investigated by using 0.03 g of NiO@HT-derived C composite mixed with 25 mL of MR dye solution ( $10\text{--}200 \text{ mg L}^{-1}$ ) at pH 2.5 and a contact time of 2 h at room temperature.

## 3. Results and discussion

### 3.1. Materials characterization

X-ray diffraction (XRD) was used to investigate the structure of the prepared materials. As shown in Fig. 2a, the XRD pattern of the NiO@HT-derived C composite showed diffraction peaks at  $2\theta$  of  $37.1^\circ$ ,  $43.2^\circ$ ,  $63^\circ$ ,  $73.5^\circ$ , and  $79.6^\circ$ , all assigned to cubic-centered NiO (JCPDS 47-1049). In addition, two diffraction peaks for carbon were observed at around  $22.5^\circ$  and  $40^\circ$ .

This indicates that NiO nanoparticles were successfully doped onto the carbon phase.<sup>34,35</sup>

The FT-IR spectra of the HT powder and NiO@HT derived C samples are presented in Fig. 2b. The HT spectrum showed a broad band at  $3405 \text{ cm}^{-1}$  for the OH groups, which can be assigned by absorbing water molecules from the atmosphere. The small band located at  $2935 \text{ cm}^{-1}$  is for the asymmetric and symmetric stretching vibration of C–H bonds. However, the bands at  $1740$  and  $1625 \text{ cm}^{-1}$  are attributed to the carbonyl (C=O) and the C=C groups, respectively.<sup>36</sup> The symmetric stretching of the carboxylate group (COO<sup>–</sup>) is assigned to the next small band at  $1370 \text{ cm}^{-1}$ . The peak at  $1255 \text{ cm}^{-1}$  is assigned to the deformation vibration of C=O and the stretching formation of OH of carboxylic acids and phenols, while the peak at  $1050 \text{ cm}^{-1}$  corresponds to the C–O band in the –OCH<sub>3</sub> groups of lignin. For the NiO@HT-derived C composite, all peaks of the HT have been observed and the peak at  $1050 \text{ cm}^{-1}$  becomes much stronger, which indicates the bonding between Ni<sup>2+</sup> ions and the functional groups of lignin present in the HT.<sup>37,38</sup>

The XPS survey scan of the NiO@HT derived C composite in Fig. 3c demonstrates the presence of Ni, O, and C elements, which confirms the formation of the NiO@HT-derived C composite. Fig. 3d–f shows the Ni 2p, O 1s, and C 1s peaks, which were evaluated using XPS peak version 4.1 software.

As shown in Fig. 2d, the Ni 2p spectrum shows five fitted peaks. These peaks are  $2p_{3/2}$  (856.9 eV) and its satellites (858.3 and 862.2 eV), and  $2p_{1/2}$  (874.5 eV) and its satellite (880.2 eV). The difference in binding energy between Ni  $2p_{3/2}$  and Ni  $2p_{1/2}$



is 17.6 eV. All these peaks are characteristic of  $\text{Ni}^{2+}$ , revealing the presence of  $\text{NiO}$ .<sup>39,40</sup> The C1s spectrum in Fig. 2e has four distinct peaks at 284.6, 285.5, 286.8 and 289.2 eV for non-oxygenated carbon atoms (C–C), carbon atoms in C–OH or C–O–Ni bands, carbon in carboxyl groups (C=O) and carbon in carboxyl hyaluronic acid (HO–C=O), respectively. The XPS profile of O1s (Fig. 2f) displayed two deconvoluted peaks. The one located at lower binding energy (531.2 eV) is assigned to the oxygen bonded with the O–Ni band, showing that oxygen bridges should be C–O–Ni bands, while the higher one at 532.4 eV is for the physically adsorbed oxygen.

The morphology of the  $\text{NiO}@\text{HT}$ -derived C composite was investigated by TEM/HR TEM and SAED measurements. As shown in TEM images (Fig. 3a and b), small dark dots can be visible, revealing that the  $\text{NiO}$  nanoparticles were equally distributed on the surface of the carbon matrix.<sup>41</sup> The HR TEM image of the  $\text{NiO}@\text{HT}$ -derived C composite (Fig. 3c) shows a lattice fringe with an interplanar spacing of 0.24 nm, which matches the (111) planes of  $\text{NiO}$ . The SAED profile in Fig. 3d displays several distinct diffraction rings that correspond to the (111), (200), (220), (311), and (222) planes, with interplanar spacings that match the JCPDS 47-1049 ( $\text{NiO}$ ) card data.<sup>41</sup>

The surface area and porous structure are important factors for providing more active sites, which promote the adsorption process.<sup>42</sup> The nitrogen adsorption–desorption isotherm of the  $\text{NiO}@\text{HT}$ -derived C composite is presented in Fig. S1a (ESI†).

Based on the IUPAC classifications, the  $\text{NiO}@\text{HT}$ -derived C composite exhibits a type-II isotherm with an H3 hysteresis loop. This is typical of micro/mesoporous materials composed of aggregates of particles creating slit-shaped pores.<sup>43</sup> Micropore adsorption is responsible for the rapid increase in nitrogen absorption capacity at low pressure ( $P/P_0 = 0\text{--}0.01$ ).<sup>43</sup> The presence of mesoporous structures is demonstrated by an increase in nitrogen absorption capability. The specific surface area ( $S_{\text{BET}}$ ) of the  $\text{NiO}@\text{HT}$ -derived C composite was estimated to be  $141 \text{ m}^2 \text{ g}^{-1}$  using the BET-equation in the pressure range of applicability ( $P/P_0 = 0.05\text{--}0.30$ ). The large surface area provides more adsorption sites and large contact area with the solution, resulting in improved overall adsorption efficiency.<sup>42</sup> The Barrett–Joyner–Halenda (BJH) method pore size distribution shown in Fig. S1b (ESI†). The pore size distribution curve showed that the  $\text{NiO}@\text{HT}$ -derived C composite is mesoporous, which is ideal for dye adsorption.<sup>12</sup>

### 3.2. Adsorption studies

**3.2.1. Adsorption capacities of the adsorbent materials.** The adsorption capacity of both HT-derived C and  $\text{NiO}@\text{HT}$ -derived C composites was determined at different MR concentrations. From the obtained data in Fig. 4a, it can be observed that the adsorption capacities of both adsorbents were significantly enhanced with increasing MR dye concentration. The  $q_e$  of the  $\text{NiO}@\text{HT}$ -derived C composite and HT-derived C increased from

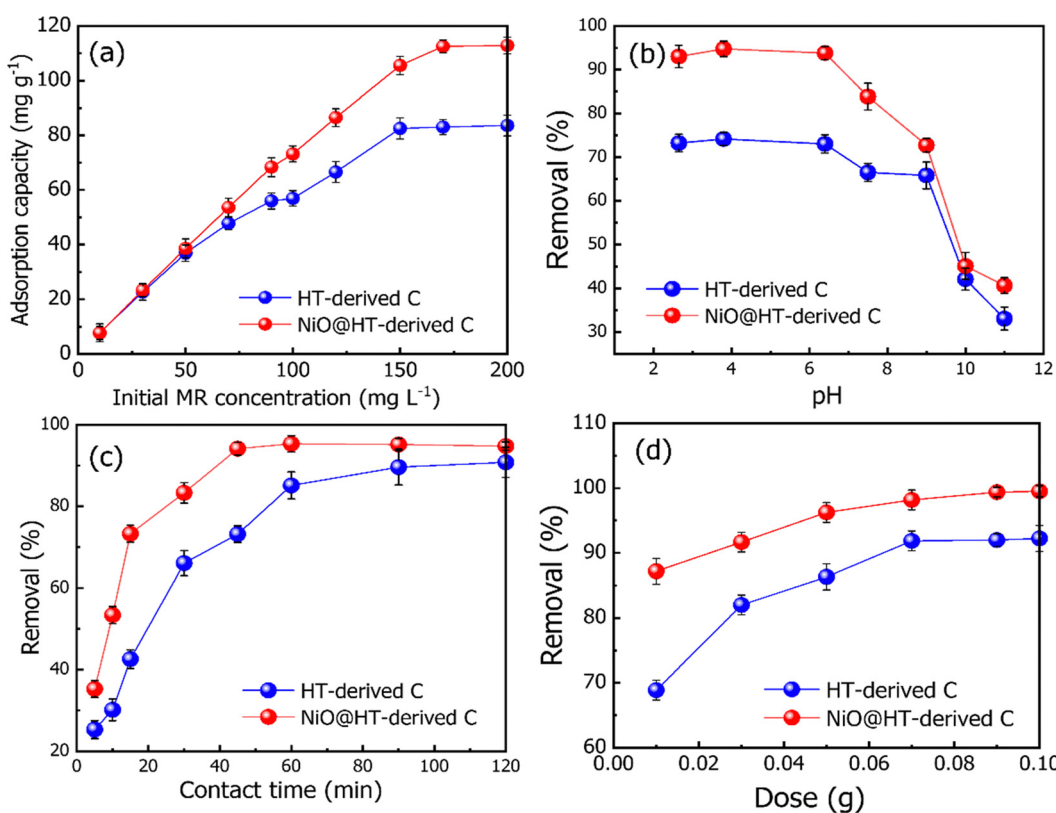


Fig. 4 Effect of (a) initial dye concentration [ $M = 0.03 \text{ g}$ ,  $t = 60 \text{ min}$ ,  $\text{pH} = 2.5$ ], (b) solution pH [ $C_0 = 50 \text{ mg L}^{-1}$ ,  $M = 0.03 \text{ g}$ ,  $t = 45 \text{ min}$ ,  $\text{pH} = 2.5\text{--}11$ ], (c) contact time [ $M = 0.03 \text{ g}$ ,  $C_0 = 50 \text{ mg L}^{-1}$ ,  $\text{pH} = 2.5$ ] and (d) adsorbent dosage [ $M = 0.01\text{--}0.1 \text{ g}$ ,  $C_0 = 50 \text{ mg L}^{-1}$ ,  $\text{pH} = 2.5$ ] on the removal of the MR dye from aqueous solution.



7.89 to 112.84 mg g<sup>-1</sup>, and 6.57 to 83.44 mg g<sup>-1</sup>, respectively, by increasing the MR concentration from 10 to 200 mg L<sup>-1</sup>. It has been reported that the increasing concentration of the dye boosts the mass transfer driving force *via* several collisions between dye molecules and the surface of the adsorbent at the initial stages of the adsorption process.<sup>44</sup> On the other hand, by increasing the MR concentration from 10 to 200 mg L<sup>-1</sup>, the removal percentages of the NiO@HT-derived C composite and HT-derived C declined from 94.64 to 67.70%, and 90.78 to 57.21%, respectively (Table S1, ESI<sup>†</sup>). This is mainly attributed to the rising repulsion forces between the MR molecules on the surface of the adsorbent and the bulk phase after the initial adsorption.<sup>44,45</sup> Overall, the adsorption capacity of the NiO@HT-derived C composite is much higher than that of the HT-derived C composite, which is mainly due to the higher surface area and porous structures.<sup>46,47</sup>

**3.2.2. Effect of pH.** The pH of the solution plays a non-dispensable role in the overall adsorption progress. Experiments were performed with an adsorbent dosage of 0.03 g per 25 mL, an initial MR dye concentration of 50 mg L<sup>-1</sup>, at a contact time of 45 min, and at various pH values from 2.5 to 11 at room temperature. As shown in Fig. 4b, the removal percentage of the MR dye on HT-derived C and NiO@HT-derived C composites decreased with the solution pH from pH 2.5 to pH 11, which means that at pH of 2.5 both materials removed most of the MR dye. The removal percentage (adsorption capacity) at pH 2.5 was 92.24% (38.89 mg g<sup>-1</sup>) and 72.26% (30.20 mg g<sup>-1</sup>) for the NiO@HT-derived C composite and HT-derived C, respectively. The adsorbent materials are positively charged at acidic pH, causing a significant electrostatic attraction between the anionic dye molecules and the positively charged functional groups on the adsorbent powder, resulting in increased MR dye adsorption efficiency at lower pH. On the other hand, the decrease in dye removal at higher pH can be attributed to the high competition for adsorption sites on the surface of the adsorbent between the presence of excess OH<sup>-</sup> ions in the aqueous solution and the anionic groups of the MR dye.<sup>48</sup> It has been extensively reported in the literature that the adsorption effectiveness of anionic dyes diminishes with increasing pH,<sup>9,49,50</sup> but the adsorption efficiency of cationic dyes

increases with increasing pH.<sup>51</sup> According to Ahmed *et al.*<sup>11</sup> the highest MR dye adsorption using activated Lemongrass leaves was achieved at pH  $\approx$  2. Enenebeaku *et al.*<sup>48</sup> also showed that white potato peels removed 90.5% of MR dye at pH 2.

**3.2.3. Effect of adsorbent dosage.** The effect of various dosages of the adsorbent on the removal of the MR dye from aqueous solutions was investigated and is presented in Fig. 4d. Variable adsorbent amounts ranging from 0.01 to 0.1 g are applied to study the adsorption of the MR dye with 50 mg L<sup>-1</sup> as the initial concentration, at a contact time of 45 min, a pH of 2.5, at room temperature and a constant pH of 2.5. As presented in Fig. 4d, when the adsorbent dose increased from 0.01 to 0.1 g, the removal percentage (adsorption capacity) of the MR dye gradually increased from 87.18% (36.32 mg g<sup>-1</sup>) to 99.50% (41.67 mg g<sup>-1</sup>) for the NiO@HT-derived C composite, and from 68.84% to 92.23% for HT-derived C. The increase in MR removal may be attributed to the increase in the number of available adsorption sites.

**3.2.4. Effect of contact time.** One of the most critical parameters for determining the design of wastewater treatment systems is equilibrium time. The impact of the adsorption period on the adsorption capacity of the prepared materials was investigated by preparing various MR solutions (50 mg L<sup>-1</sup>) at a pH of 2.5. The prepared dye solutions were stirred with 0.03 g of adsorbent material at room temperature for various contact times ranging from 5 to 120 min. As observed from Fig. 4c, the removal percentage (adsorption capacity) increased from 32.93% (13.73 mg g<sup>-1</sup>) to 95.17% (40.37 mg g<sup>-1</sup>) for the NiO@HT-derived C composite, and from 25.33% (10.73 mg g<sup>-1</sup>) to 90.80% (37.82 mg g<sup>-1</sup>) for the HT-derived C composite. The presence of many vacant active sites on the adsorbent surface may have contributed to the initial acceleration of the MR dye adsorption in the early stage. (*i.e.*, until a contact time of 60 min). However, after that, the adsorption reached a plateau because there were gradually fewer accessible adsorption sites and more repulsive interactions between the MR molecules on the adsorbent and the bulk phase.<sup>52</sup>

**3.2.5. Adsorption kinetics.** MR sorption kinetics presented in Fig. 5 reveals that adsorption was rapid at the early stage

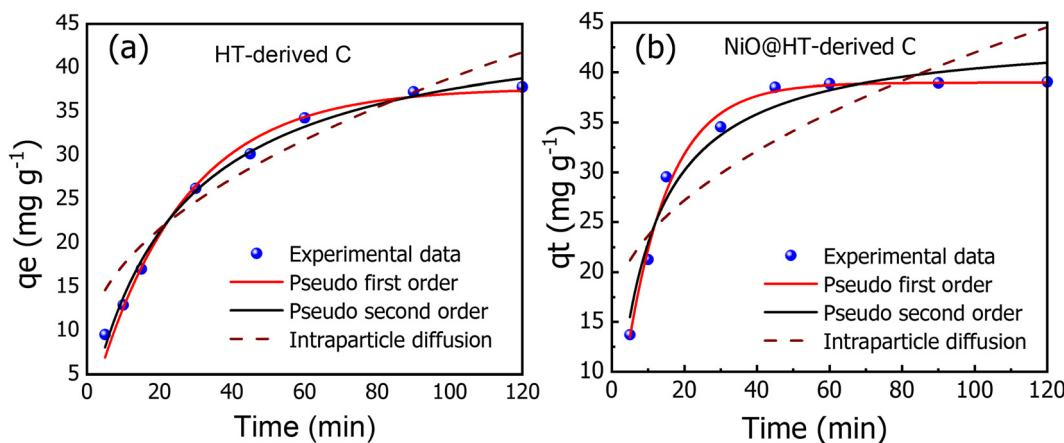


Fig. 5 The experimental and kinetic adsorption models for the adsorption of MR onto (a) HT-derived C and (b) NiO@HT-derived C adsorbents [ $C_0 = 50 \text{ mg L}^{-1}$ ,  $M = 0.03 \text{ g}$ , pH = 3,  $t = 5\text{--}120 \text{ min}$ ].



(at 30 min) followed by slightly decreasing and plateaued after 60 min. Three kinetic models, namely pseudo-first-order, pseudo-second order, and intra-particle diffusion models, were investigated in the nonlinear regression to examine the kinetic behavior of the MR dye adsorbed on the adsorbents under investigation.

The pseudo-first-order kinetic model is described by eqn (3).<sup>53</sup>

$$q_t = q_e(1 - e^{-k_1 t}) \quad (3)$$

where  $q_e$  and  $q_t$  are the MR dye adsorbed ( $\text{mg g}^{-1}$ ) at equilibrium and at time  $t$  (min), respectively.  $k_1$  is the rate constant of the pseudo-first-order kinetic model ( $\text{min}^{-1}$ ).

The pseudo-second-order kinetic model is given by eqn (4).

$$q_t = \frac{q_e^2 k_2 t}{1 + k_2 q_e t} \quad (4)$$

where  $k_2$  is the rate constant of the pseudo-second-order kinetic model ( $\text{g mg}^{-1} \text{min}^{-1}$ ).

Neither the pseudo-first order nor the second-order model could identify the rate-limiting step. Therefore, an intra-particle mass transfer diffusion model proposed by Weber and Morris was used (eqn (5)).<sup>54</sup>

$$q_t = k_{\text{diff}} t^{0.5} + C \quad (5)$$

where  $k_i$  is the intra-particle diffusion rate constant ( $\text{mg g}^{-1} \text{min}^{-1/2}$ ) and the values of  $C$  ( $\text{mg g}^{-1}$ ) indicate the boundary thickness.

The related various kinetic parameters and their correlation coefficients are listed in Table 1. It is observed that the experimental data of the adsorbed MR on HT-derived C and NiO@HT-derived C materials were fitted by the pseudo second-order model than the first order kinetic model as indicated by higher  $R^2$  values. Significantly, the predicted and experimental adsorption capabilities have a larger affinity for the pseudo second order model.

The estimated  $q_e$  values for the pseudo-second-order model were 46.477 and 44.123  $\text{mg g}^{-1}$ , for HT-derived C and NiO@HT-derived C, respectively, which are higher than those estimated for the pseudo-first order model as shown in Table 1. It is clearly observed from the fitted data in Fig. 5, and related parameters in Table 1, that the  $R^2$  values of the pseudo-first- and the pseudo second-order models displays good correlation

**Table 1** Parameters of the pseudo-first and pseudo-second-order kinetic and the intra-particle diffusion models.  $[C_0 = 50 \text{ mg L}^{-1}$ ,  $M = 0.03 \text{ g}$ ,  $\text{pH} = 3$ ,  $t = 5-120 \text{ min}$ ]

Kinetic model	Parameter	HT-derived C	NiO@HT-derived C
Pseudo-first order	$q_e (\text{mg g}^{-1})$	37.692	38.970
	$K_1 (\text{min}^{-1})$	0.041	0.085
	$R^2$	0.987	0.9905
Pseudo-second order	$q_e (\text{mg g}^{-1})$	46.477	44.123
	$K_2 (\text{g mg}^{-1} \text{min}^{-1})$	0.00091	0.00245
Intra-particle diffusion	$R^2$	0.932	0.969
	$K_{\text{diff}} (\text{mg g}^{-1} \text{min}^{-0.5})$	3.113	2.679
	$C (\text{mg g}^{-1})$	3.666	15.194
	$R^2$	0.881	0.793

with the experimental data, which indicate the presence of both physical adsorption and chemical adsorption. However, the higher  $R^2$  values confirmed that the adsorption process predominantly followed the pseudo-second-order kinetic model. It is significant to note that both physisorption and chemisorption may take place concurrently on the surface of an adsorbent, with one layer of molecules being physically adsorbed on top of the other.<sup>55</sup>

Adsorption processes are often governed by a variety of mechanisms, the most limiting of which are diffusion mechanisms, such as external diffusion and intra-particle diffusion.<sup>56</sup> As a result, the intra-particle diffusion model was investigated to estimate the rate-controlling step of the adsorption process. The intraparticle diffusion model for MR onto HT-derived C and NiO@HT-derived C adsorbents demonstrated the least fitting to experimental kinetic data. However, the plots did not also pass through the origin, implying that the adsorption process involves intra-particle diffusion rather than a sole rate-controlling process.<sup>12</sup> Thus external mass transfer and intra-particle diffusion can be used to manage the entire adsorption process. From the above discussion, it can be concluded that the pseudo-second-order model is the best model to fit the experimental data for adsorption of MR onto both materials for HT-derived C and NiO@HT-derived C adsorbents. This indicates that the rate limiting step for MR is probably the chemisorption process, thus, involving exchange of electrons between the adsorbent and adsorbate.<sup>55</sup>

**3.2.6. Adsorption isotherms.** The most popular isotherms used to characterize the solid–liquid adsorption systems are the Langmuir isotherm and the Freundlich isotherm models. The Langmuir model describes the monolayer adsorption onto a perfectly smooth and homogenous surface with a finite number of identical sites. This model is simply expressed by eqn (6).<sup>57</sup>

$$q_e = \frac{q_{\max} K_L C_e}{1 + K_L C_e} \quad (6)$$

where  $C_e$  ( $\text{mg L}^{-1}$ ) is the equilibrium concentration,  $q_{\max}$  ( $\text{mg g}^{-1}$ ) is the maximum adsorbate amount, and  $K_L$  ( $\text{L mg}^{-1}$ ) is the Langmuir constant related to the adsorption affinity of the binding sites.

The Freundlich model is another model that can be employed to describe heterogeneous surfaces and multilayer adsorption systems, and its linearized form can be given by eqn (7).<sup>54</sup>

$$q_e = K_f C_e^{1/n} \quad (7)$$

where  $q_e$  and  $C_e$  are the same as those mentioned above in the Langmuir equation.  $K_f$  ( $\text{L g}^{-1}$ ) and  $n$  are the Freundlich constants, which represent the adsorption capacity and intensity, respectively.

As shown in Fig. 6(a and b), and Table 2, the experimental data of MR adsorbed onto HT-derived C and NiO@HT-derived C composite materials can be fitted by Langmuir and Freundlich isotherms. However, the experimental data were best described by the Langmuir isotherm model as indicated by higher  $R^2$  and lower  $\chi^2$  values. This suggests that an MR dye monolayer has formed on a surface that is uniformly covered with localized adsorption sites, which was also reported in red 14 adsorption onto activated carbon derived from cherry tree waste.<sup>58</sup>

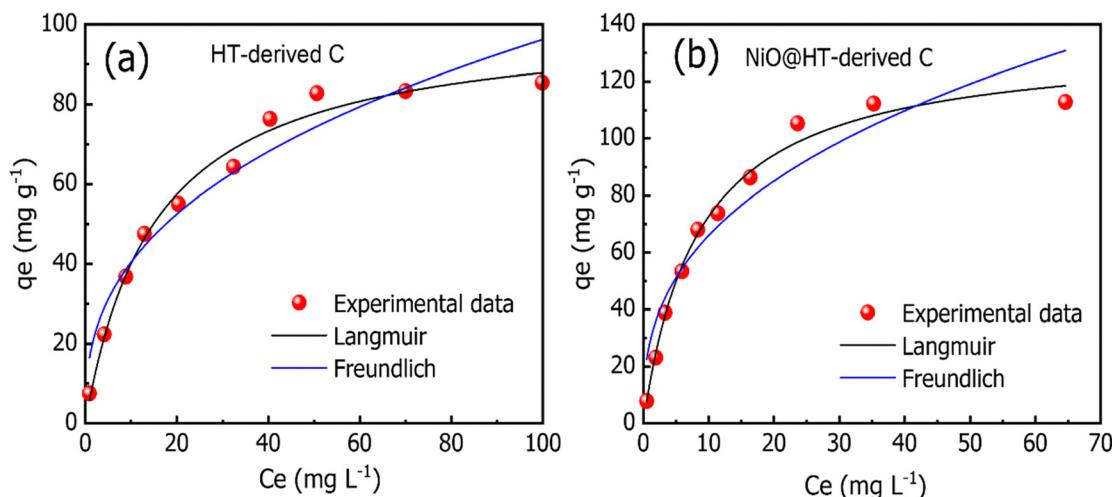


Fig. 6 The experimental and isotherm adsorption isotherm models (Langmuir and Freundlich) for adsorption of MR onto (a) HT-derived C and (b) NiO@HT-derived C materials [ $C_0 = 10\text{--}200\text{ mg L}^{-1}$ ,  $M = 0.03\text{ g}$ , pH = 3, time = 45 min].

Table 2 The parameters estimated from isotherm models for the adsorption of MR on HT-derived C and NiO@HT-derived C

Isotherm model	Parameter	HT-derived C	NiO@HT-derived C
Langmuir	$q_m\text{ (mg g}^{-1}\text{)}$	101.321	134.075
	$K_L\text{ (L mg}^{-1}\text{)}$	0.0654	0.118
	Adj. $R^2$	0.988	0.989
Freundlich	$\chi^2$	9.10	14.586
	$K_f\text{ (L g}^{-1}\text{)}$	16.975	28.300
	$N$	2.652	2.724
Freundlich	Adj. $R^2$	0.935	0.898
	$\chi^2$	48.873	140.243

The Langmuir constant  $K_L$  is usually used to describe the interaction between the adsorbate and adsorbent. As listed in Table 2, the  $K_L$  value for MR adsorption onto NiO@HT-derived C is  $0.118\text{ L mg}^{-1}$ , which is much higher than that for MR onto HT-derived C ( $0.065\text{ L mg}^{-1}$ ). This indicates that the interactions between MR and NiO@HT-derived C are more stable than

the interactions between MR and the HT-derived C. In other words, the sorbent NiO@HT-derived C has a greater affinity for MR than HT-derived C.

The estimated maximum adsorption capacities ( $\text{mg g}^{-1}$ ) of MR onto HT-derived C and NiO@HT-derived C composites are  $101.321$  and  $134.075\text{ mg g}^{-1}$ , respectively. The higher value of the maximum adsorption capacity for MR onto the NiO@HT-derived C composite than that for MR onto HT-derived C can be attributed to the higher surface area, and due to the presence of NiO nanoparticles which act as active centers for adsorption.

**3.2.7. MR desorption study.** The reusability of the adsorbent several times is a critical factor in the wastewater treatment process. Adsorption–desorption recycling of the adsorbent materials is a very important factor that should be taken into consideration for their practical applications. If the adsorbent cannot be utilised repeatedly or has a significantly reduced adsorption efficiency after repeated use, it will cause secondary environmental deterioration and be expensive for industrial

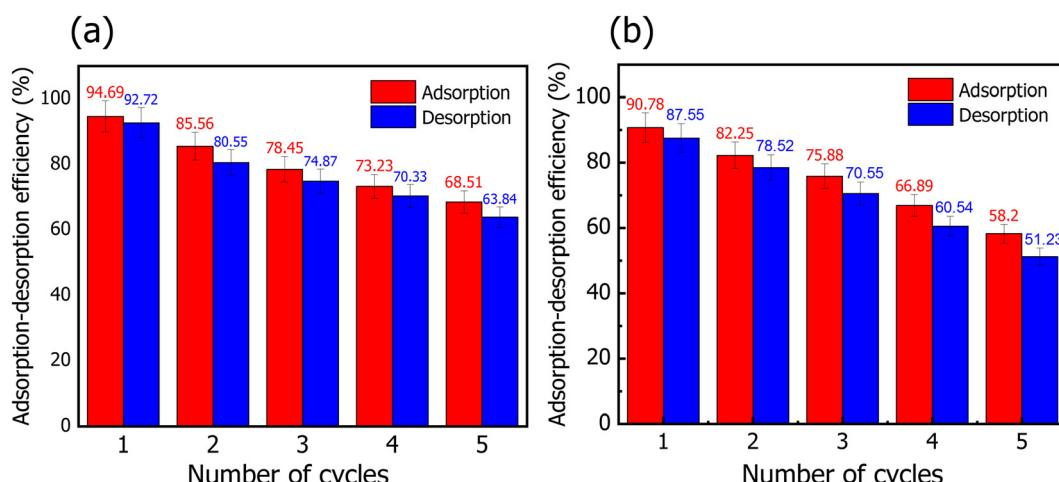


Fig. 7 Adsorption–desorption cycles of the MR dye onto (a) NiO@HT-derived C and (b) HT-derived C adsorbents.



application.<sup>59</sup> Thus, desorption of the MR dye has to be investigated as shown in Fig. 7(a and b). Over five cycles, the efficiency of MR adsorption declined from 94.69% to 63.84% and 90.78% to 51.23% for NiO@HT-derived C and HT-derived C, respectively. This is due to the loss of adsorbent materials *via* centrifugation. This reveals that our adsorbent materials could be reused several times for wastewater treatment.

## 4. Conclusions

In conclusion, a series of experiments for the absorption of MR onto HT-derived C and NiO@HT-derived C have been reported. It should be noted that the maximum adsorption capacity for MR onto NiO@HT-derived C is found to be  $129.87 \text{ mg g}^{-1}$  at pH 3. This value is much higher than that achieved by HT-derived C ( $82.82 \text{ mg g}^{-1}$ ). The equilibrium data are studied using the Langmuir and Freundlich isotherm models. Although both the Langmuir and Freundlich isotherms could be used to describe the adsorption behaviour with a high correlation coefficient, the Langmuir model fits the experimental data better. In addition, the kinetic mechanism is studied by using the pseudo first order, pseudo second order, and intra-particle diffusion models. The obtained results reveal good agreement between the experimental data and the pseudo second order kinetic model. This reveals a chemical adsorption process in which the MR adsorption over NiO@HT-derived C and HT-derived C can be explained to be through electrostatic attraction and  $\pi-\pi$  interactions. Furthermore, the recyclability tests indicate a good capability of reusing NiO@HT-derived C and HT-derived C for many cycles with no significant reduction in the adsorption capacity, revealing high ability for practical applications.

## Conflicts of interest

The authors declare that they have no known competing financial interests or personal relationships that could have appeared to influence the work reported in this paper.

## References

- 1 C. Gr  gorio, *Bioresour. Technol.*, 2006, **97**, 1061–1085.
- 2 Z. Yanbo, L. Jian, Z. Yi and L. Yongdi, *Environ. Pollut.*, 2019, **252**, 352–365.
- 3 A. J. Sunil Kumar Bajpai, *Water*, 2012, **4**, 52–57.
- 4 K. Sushila, A. Sharma, S. C. Sahoo, G. Kumar, S. K. Mehta and R. Kataria, *J. Mol. Struct.*, 2021, **1226**, 129327.
- 5 C. I. Pearce, J. R. Lloyd and J. T. Guthrie, *Dyes Pigm.*, 2003, **58**, 179–196.
- 6 Y. Zhou, J. Wang, Q. Zhao, H. Cai and H. Zhang, *Chemistry-Select*, 2022, **7**, e202203280.
- 7 R. Sunil, B. Swapnil and S. Virendra Kumar, *Ultrason. Sonochem.*, 2017, **34**, 183–194.
- 8 V. Selvaraj, T. Swarna Karthika, C. Mansiya and M. Alagar, *J. Mol. Struct.*, 2021, **1224**, 129195, DOI: [10.1016/j.molstruc.2020.129195](https://doi.org/10.1016/j.molstruc.2020.129195).
- 9 A. Mohd Azmier, A. Nur'Adilah Binti, A. Kayode Adesina and B. Olugbenga Solomon, *Chem. Data Collect.*, 2019, **22**, 100249.
- 10 M. A. Ahmad, N. Ahmad and O. S. Bello, *Appl. Water Sci.*, 2014, **5**, 407–423.
- 11 Y. Badr, M. G. Abd El-Wahed and M. A. Mahmoud, *J. Hazard. Mater.*, 2008, **154**, 245–253.
- 12 R. Sunil, S. Virendra Kumar, P. Avdesh Singh, N. Mohit and R. Kuldeep, *Curr. Res. Green and Sustainable Chem.*, 2021, **4**, 100180.
- 13 M. Riera-Torres, C. Guti  rrez-Bouz  n and M. Crespi, *Desalination*, 2010, **252**, 53–59.
- 14 G.-M. Julia, R. Nilbia, M. Iv  n, D. Xavier, A. G.-H. Jos  , T. Francesc and P. Jos  , *J. Hazard. Mater.*, 2006, **138**, 218–225.
- 15 W. Jiangning, A. E. Mark and S. E. Law, *J. Environ. Eng.*, 1998, **124**, 272–277.
- 16 S. Venkata Mohan, P. Sailaja, M. Srimurali and J. Karthikeyan, *Environ. Eng. Policy*, 1998, **1**, 149–154.
- 17 C.-H. Wu and J.-M. Chern, *Indust. Eng. Chem. Res.*, 2006, **45**, 6450–6457.
- 18 K. Equbal Ahmad Shahjahan and K. Tabrez Alam, *J. Mol. Liq.*, 2018, **249**, 1195–1211.
- 19 K. Amel, B. Esma Mahfouf, D. Kerroum, B. Souheila, C. Bouchra and B. Raouf, *Cleaner Chem. Eng.*, 2022, **4**, 100069.
- 20 S. Gul, M. Kanwal, R. A. Qazi, H. Gul, R. Khattak, M. S. Khan, F. Khitab and A. E. Krauklis, *Water*, 2022, **14**, 2831.
- 21 N. M. Hosny, I. Gomaa and M. G. Elmahgary, *Appl. Surf. Sci. Adv.*, 2023, **15**, 100395.
- 22 Z. Muhammad Nadeem, D. Qamar, N. Faisal, Z. Muhammad Naveed, I. Munawar and N. Muhammad Faizan, *J. Mater. Res. Technol.*, 2019, **8**, 713–725.
- 23 A. S. A. Ahmed, W. Xiang, M. Abdelmotalleib and X. Zhao, *ACS Appl. Electron. Mater.*, 2022, **4**, 1063–1071.
- 24 N. Arailym, C. Moon Ho, K. Jik-Soo, M. Seung-Taek, K. Sung-Soo and S. Yang-Kook, *J. Power Sources*, 2015, **299**, 425–433.
- 25 Y. Abdelbaki, A. de Arriba, R. Issaadi, R. S  nchez-Tovar, B. Solsona and J. M. L  pez Nieto, *Fuel Process. Technol.*, 2022, **229**, 107182.
- 26 Q. Riaz, M. Ahmed, M. N. Zafar, M. Zubair, M. F. Nazar, S. H. Sumirra, I. Ahmad and A. Hosseini-Bandegharaei, *Int. J. Environ. Anal. Chem.*, 2020, **102**, 84–103.
- 27 T. Zhu, J. S. Chen and X. W. Lou, *J. Phys. Chem. C*, 2012, **116**, 6873–6878.
- 28 M. A. El-Ghobashy, H. Hashim, M. A. Darwish, M. U. Khandaker, A. Sulieman, N. Tamam, S. V. Trukhanov, A. V. Trukhanov and M. A. Salem, *Nanomaterials*, 2022, **12**.
- 29 M. R. Al-Bahrani, W. Ahmad, H. F. Mehnane, Y. Chen, Z. Cheng and Y. Gao, *Nanomicro Lett.*, 2015, **7**, 298–306.
- 30 S. Joshi, S. Shrestha and B. Shrestha, *Chem. Eng. Technol.*, 2021, **44**, 2327–2332.
- 31 H. N. Hamad and S. Idrus, *Polymers*, 2022, **14**.
- 32 A. S. Al-Wasidi, I. I. S. AlZahrani, H. I. Thawibaraka, A. M. Naglah, M. G. El-Desouky and M. A. El-Bindary, *J. Mol. Struct.*, 2022, **1250**, 131736.
- 33 E. G. Magdi, Z. Nana, Y. Yanbin, L. Pansheng, W. Shoujuan, T. Tamrat and K. Fangong, *J. Cleaner Prod.*, 2020, **267**, 121949.



34 M. Patange, S. Biswas, A. K. Yadav, S. N. Jha and D. Bhattacharyya, *Phys. Chem. Chem. Phys.*, 2015, **17**, 32398–32412.

35 H. Wang, Y. Zhang, Q. Wang, C. Jia, P. Cai, G. Chen, C. Dong and H. Guan, *RSC Adv.*, 2019, **9**, 9126–9135.

36 F. Yang, Y. He, S. Sun, Y. Chang, F. Zha and Z. Lei, *J. Appl. Poly. Sci.*, 2016, 133.

37 D. Cholico-Gonzalez, N. Ortiz Lara, A. M. Fernandez Macedo and J. Chavez Salas, *ACS Omega*, 2020, **5**, 3302–3314.

38 N. Azouaou, Z. Sadaoui, A. Djaaifi and H. Mokaddem, *J. Hazard. Mater.*, 2010, **184**, 126–134.

39 W. Liu, C. Lu, X. Wang, K. Liang and B. K. Tay, *J. Mater. Chem. A*, 2015, **3**, 624–633.

40 N. Jayababu, M. Poloju, J. Shruthi and M. V. R. Reddy, *RSC Adv.*, 2019, **9**, 13765–13775.

41 A. A. L. M. I. Chebanenko, V. N. Nevedomskiy and V. I. Popkov, *Dalton Trans.*, 2020, **49**, 12088–12097.

42 H. Frost, T. Düren and R. Q. Snurr, *J. Phys. Chem. B*, 2006, **110**, 9565–9570.

43 M. Thommes, K. Kaneko, A. V. Neimark, J. P. Olivier, F. Rodriguez-Reinoso, J. Rouquerol and K. S. W. Sing, *Pure Appl. Chem.*, 2015, 87.

44 K. Mensah, H. Mahmoud, M. Fujii, M. Samy and H. Shokry, *Biomass Convers. Biorefin.*, 2022, DOI: [10.1007/s13399-022-03304-4](https://doi.org/10.1007/s13399-022-03304-4).

45 S. Hassan, E. Marwa and H. Hesham, *J. Mater. Res. Technol.*, 2019, **8**, 4477–4488.

46 P. S. S. Venkata Mohan, M. Srimurali and J. Karthikeyan, *Environ. Eng. Pol.*, 1999, **1**, 149–154.

47 N. Hassan, A. Shahat, A. El-Didamony, M. G. El-Desouky and A. A. El-Binary, *J. Mol. Struct.*, 2020, **1210**, 128029.

48 C. K. Enenebeaku, N. J. Okorocha, U. E. Enenebeaku and I. C. Ukaga, *Inter. Lett. Chem. Phys. Astron.*, 2017, **72**, 52–64.

49 M. F. Elkady, M. I. Amal and M. M. A. El-Latif, *Desalination*, 2011, **278**, 412–423.

50 S. Dadfarnia, A. M. S. E. Moradi and S. Emami, *Appl. Surf. Sci.*, 2015, **330**, 85–93.

51 D. Mehmet and A. Mahir, *Chemosphere*, 2003, **50**, 517–528.

52 Y. Liu, C. Luo, J. Sun, H. Li, Z. Sun and S. Yan, *J. Mater. Chem. A*, 2015, **3**, 5674–5682.

53 H. Y. Zhu, R. Jiang, L. Xiao and G. M. Zeng, *Bioresour. Technol.*, 2010, **101**, 5063–5069.

54 C. G. Ramos, S. A. Sousa, A. M. Grilo, J. R. Feliciano and J. H. Leitão, *J. Bacteriol.*, 2014, **196**, 3980.

55 A. Denizli, R. Say and Y. Arica, *Sep. Purif. Technol.*, 2000, **21**, 181–190.

56 A. Ozcan, E. M. Oncü and A. S. Ozcan, *J. Hazard. Mater.*, 2006, **129**, 244–252.

57 I. Langmuir, *J. Am. Chem. Soc.*, 1918, **40**, 1361–1403.

58 R. Askari, F. Mohammadi, A. Moharrami, S. Afshin, Y. Rashtbari, M. Vosoughi and A. Dargahi, *Appl. Water Sci.*, 2023, **13**, 90.

59 N. Ghosh, S. Sen, G. Biswas, A. Saxena and P. K. Haldar, *Water, Air, Soil Pollut.*, 2023, **234**, 202.

